

# Experimental Investigations on Aggregate–Aggregate Collisions in the Early Solar Nebula

JÜRGEN BLUM<sup>1</sup> AND MICHAEL MÜNCH

Max-Planck-Institut für Kernphysik, Postfach 103980, D-69029 Heidelberg, Germany  
E-mail: jblum@kosmo.mpi-hd.mpg.de

Received February 3, 1993; revised May 10, 1993

Low-velocity aggregate–aggregate collisions play an important role for the development of aggregate sizes during the first stages of accumulation of solid bodies in the preplanetary nebula. To study such collisions, an experimental setup was developed where two millimeter-sized dust aggregates collide in vacuum with relative velocities between  $\sim 0.15$  and  $\sim 4$  m sec<sup>-1</sup>. The impact parameters of the collisions are arbitrary so that central collisions as well as grazing collisions can be investigated. Two types of aggregates were used, (1) ZrSiO<sub>4</sub> with constituent particle sizes  $\leq 1$   $\mu$ m and 74% porosity and (2) Aerosil 200 (SiO<sub>2</sub>) with constituent particle sizes  $\sim 12$  nm and 97% porosity. The collision experiments were carried out in five narrow velocity windows in the above velocity regime for equal-sized aggregates (ZrSiO<sub>4</sub>(I), Aerosil 200) as well as for aggregates with a mean mass ratio of  $\sim 66$  (ZrSiO<sub>4</sub>(II)). Coagulation (i.e., sticking) of the aggregates was not observed. Low-velocity collisions resulted in restitution (i.e., bouncing), and at higher velocities, a transition from restitution to fragmentation was observed at  $v \sim 1$  m sec<sup>-1</sup> for ZrSiO<sub>4</sub>(I), as well as at  $v \sim 4$  m sec<sup>-1</sup> for Aerosil 200. For ZrSiO<sub>4</sub>(II), fragmentation at  $v \sim 4$  m sec<sup>-1</sup> was found in two cases only. Due to the lower transition velocity, the fragmentation of ZrSiO<sub>4</sub>(I) was investigated in more detail. The abundance of smaller fragments increases with increasing velocity and with decreasing impact parameter. At  $v \sim 4$  m sec<sup>-1</sup>, the fragment numbers follow a power law mass distribution  $\nu(m)dm \sim m^{-9/8} dm$ . Extrapolation of the fragment mass distribution for catastrophic collisions between equal-sized aggregates were performed using a simple fragmentation model based on the following assumptions: (1) power law mass distribution between the constituent particle mass and the aggregate mass, (2) fragments have constant free surface energies per unit surface area, and (3) impact parameter-dependent efficiency for the transition of kinetic collision energy into free surface energy of the fragments. This model predicts a complete disintegration of the ZrSiO<sub>4</sub>(I) aggregates into their building blocks for collision velocities of  $\geq 50$  m sec<sup>-1</sup>. For aggregates consisting of van der Waals-bonded constit-

uent particles of  $0.1$   $\mu$ m radii, these catastrophic collision velocities are much smaller and are predicted to be  $\sim 3$  m sec<sup>-1</sup>. These are typical velocities for the preplanetary nebula, so catastrophic fragmentations could be frequent events if aggregates in the solar nebula formed due to weak surface forces. © 1993 Academic Press, Inc.

## 1. INTRODUCTION

The formation of planetesimals in the early solar accretion disk by accumulation of presolar dust grains or of nebula condensates is generally accepted. This can, in principal, happen in two different ways: (1) Safronov (1969) and Goldreich and Ward (1973) attribute the formation of planetesimals to gravitational instabilities in a thin midplane dust layer of the disk. For this spontaneous process, the physical or chemical properties of the dust grains are unimportant, but the conditions in the nebula gas are crucial for the occurrence of the so-called *Goldreich–Ward instability*: the nebula gas has to be quiescent to allow for the sedimentation of the dust grains toward the disk's midplane and hence to form a dense dust layer.

However, it was argued that the solar nebula was turbulent, and such turbulence would alter the above scenario considerably. Völk *et al.* (1980) first calculated the influence of a Kolmogoroff-type global disk turbulence on the random gas velocity and hence, due to gas drag forces, on the random dust grain velocities as well as on root mean square collision velocities of dust particles. Weidenschilling (1984) argued that due to the large dust opacity energy released by disk accretion cannot be radiated away but causes convection of the nebula gas. These convective instabilities, in turn, drive turbulence of the nebula gas and thus greatly increase the rate of grain–grain collisions. Cabot *et al.* (1987) estimated gas turbulent velocities of  $10^{-2}$  to  $10^{-4}$  of the sound speed for the solar nebula where convection is assumed to be the sole source of turbulence. Even such low random gas velocities are sufficient to prevent the dust layer from becoming gravita-

<sup>1</sup> Present address: MPG Research Group "Dust in Star-Forming Regions," Schillerergässchen 2-3, D-07745 Jena, Germany.

Presented at the Planet Formation program held at the Institute for Theoretical Physics of the University of California at Santa Barbara, in Fall 1992.

tionally unstable (Weidenschilling 1988). In this case, preplanetesimals may form only by *coagulation* or *aggregation* of colliding grains. Mutual collisions between dust particles are caused by the turbulence of the nebula gas or by different settling or drift velocities of unequal-sized grains. Weidenschilling and Cuzzi (1993) calculated relative grain-grain velocities for different turbulence strength scenarios. For millimeter-sized grains, these relative velocities are in the centimeter per second to meter per second range.

The outcome of such low-velocity dust-dust collisions are fairly unknown. Donn and Meakin (1989) argue that successive collisions between low-density (fractal) aggregates lead to the compaction of the aggregates and in the case of a collision between grains of very dissimilar sizes to the embedding of the smaller aggregate into the larger one, and, consequently, to a mass gain of the larger body. Donn *et al.* (1991) report on experiments in which styrofoam spheres have been dropped onto powders of different materials and constituent particle sizes. They observed partial embedding of the styrofoam sphere into the dust samples as well as a compaction zone in front of the projectile. If this simulation is representative for preplanetary dust collisions—styrofoam is a rigid material—is unclear.

In an earlier work (Blum 1990), we experimentally investigated collisions between millimeter-sized fluffy aggregates composed of paraffin wax-coated glass spheres (40–80  $\mu\text{m}$  diameter). In the velocity range from 0.27 to 3.3  $\text{m sec}^{-1}$ , we observed coagulation (with increasing coagulation probability for decreasing collision velocity) as well as restitution and fragmentation (with increasing fragmentation probability for increasing collision velocity). The occurrence of coagulation is attributed to the fact that a substantial amount of soft paraffin wax (melting point 53°C) was coating the grain surfaces, leading to an attractive force-driven flattening of the constituents (Dahneke 1972). Calculations show (Blum 1990) that for harder constituent materials (e.g., for solid water ice) the coagulation limit  $v_c$  falls orders of magnitude below the experimental limits ( $v_c \sim 10^{-3} \text{ m sec}^{-1}$  for millimeter-sized water ice aggregates).

For a sticking probability of unity, Mizuno *et al.* (1988) calculated the time-dependent mass distribution of the dust grains. On the assumptions of (1) strong turbulence, (2) nonfractal aggregates, and (3) no grain fragmentation, they showed that a relatively narrow grain mass distribution results. With increasing time  $t$ , the grain mass corresponding to the peak value of the distribution grows approximately proportional to  $t^6$  (see also Markiewicz and Blum 1993). This narrow grain mass distribution function means that on the above-mentioned assumptions the process dominating the growth of dust particles is the collision between grains of similar sizes.

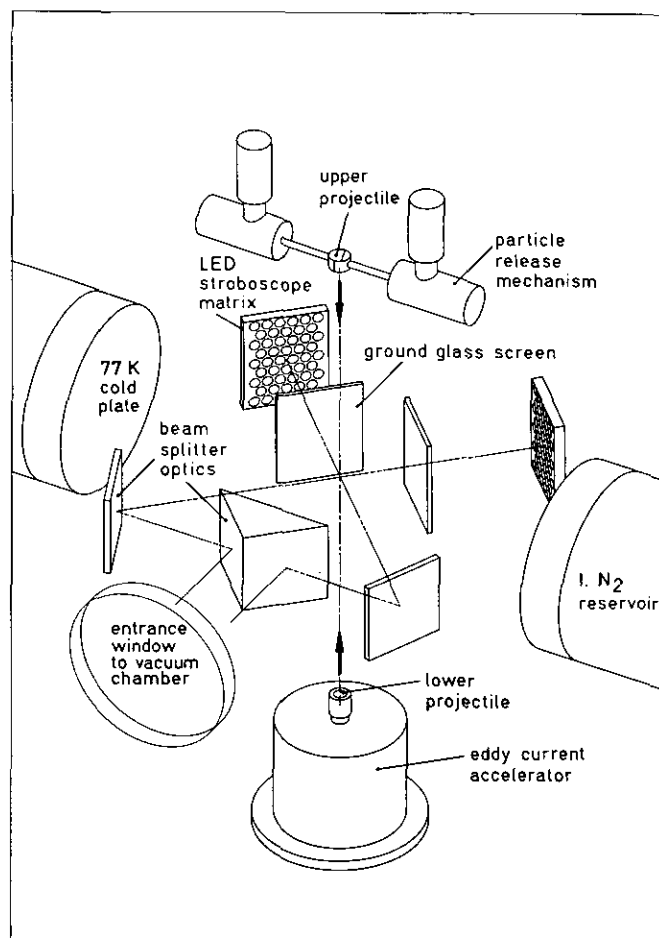


FIG. 1. Schematic view of the experimental setup for the low-velocity collisions of millimeter-sized aggregates.

In this paper, we investigate experimentally low-velocity collisions between roughly equal-sized dust aggregates. In Section 2, we present our experimental setup for the investigation of these collisions. In Section 3, we discuss the properties of the low-density aggregates we used. Details of the experimental parameters are shown in Section 4, and the experimental results are presented in Section 5. We discuss these results in Section 6, and Section 7 deals with modeling disruptive aggregate-aggregate collisions as well as with predictions for the outcome of aggregate-aggregate collisions at different velocities.

## 2. EXPERIMENTAL TECHNIQUE

We have developed an experimental setup which allows us to investigate low-velocity collisions (collision velocities range from 0.1 to 5  $\text{m sec}^{-1}$ ) between two free-falling particles (particle sizes range from 0.2 to 5 mm) in vacuum (see Fig. 1). One of the projectiles is placed on top of an electromagnetic (eddy current) accelerator based on the

principle described by Lell *et al.* (1983). Due to various guide tubes, the vertical upward direction of this particle is very well predetermined. The velocity of this projectile can be adjusted by an appropriate capacitor bank discharge voltage to values up to  $5 \text{ m sec}^{-1}$ . The other colliding particle is centered in a device which releases this projectile to free fall when an electric current is applied. Thus, both particles are in free fall during the collision, so that the collisions can be treated as zero-gravity experiments. Collisions with arbitrary impact parameters and between particles of (almost) arbitrary materials or compositions such as extremely fragile dust aggregates can be studied.

Observations of the pre- and postcollisional phases are performed by means of a digital single-frame CCD (charge-coupled device) camera with macrooptics and back-lighted stroboscopic illumination using light-emitting diodes (LEDs) as light sources. The drawback of stroboscopic illumination—the subsequent images are superimposed—has been compensated by the implementation of a dynamic brightness pattern of the LED flashes which makes image analysis considerably easier: each collision event is illuminated by a series of up to four stroboscope flashes (in general two flashes before and two flashes after the collision), each subsequent flash having twice the brightness intensity of the preceding flash. This binary-coded flash intensity mode allows maximum flash repetition frequencies of  $\sim 100 \text{ kHz}$  and due to the 1:2:4:8 intensity pattern, the superimposed images can be extracted automatically with computer aid.

Plane mirror beam-splitter optics enables simultaneous imaging from two orthogonal directions so that full three-dimensional information of each single collision is available. The accelerator, particle release mechanism, stroboscope, and beam splitter optics are contained inside a vacuum chamber. The nominal gas pressure during the experiment performance is  $\lesssim 10^{-2} \text{ mbar}$ , the ambient temperature is  $\sim 300 \text{ K}$ . Thus, the Knudsen number  $\text{Kn}$ , i.e., the ratio of the mean free path of the gas molecules  $\lambda$  to the size of the projectiles  $r$ , is  $\text{Kn} = \lambda/r \gtrsim 1$ , which means that the dust-gas interaction is in the free molecular flow regime, so that continuum flow effects such as gas flow-induced coagulation (Miller and Clark 1987) are negligible. Image analysis of the digital images (12-bit-intensity resolution) starts with an intensity adjustment for all CCD picture elements (pixels) by applying a simple flat-field algorithm to each pixel  $i$ ,

$$a_i = \frac{\text{total flash intensity}_i - \text{image intensity}_i}{\text{total flash intensity}_i - \text{dark image intensity}_i}, \quad (1)$$

where  $i = 1, \dots, 384 \times 576$  is the pixel number. In addition to the image taken during the collision, two other

frames, i.e., the total flash intensity image with no particles but the complete number of flashes and a dark image with no particles and no stroboscopic illumination, are recorded. Except for noise effects and for particle edges, the relative intensity of each pixel  $a_i$  can only take the discrete values  $0, 1/15, 2/15, \dots, 14/15, 1$  depending on the amount of shadowing by single or multiple particle covering. In a first run of the numerical image evaluation, the four subsequent raw images taken at the times  $T_1, T_2, T_3$ , and  $T_4$  are reconstructed. In general, the LED flash intensities are sufficiently large so that photon noise and CCD dark current noise are negligible. Thus, in a second evaluation run, the above-mentioned edge effects arising from incomplete pixel covering at the particles' boundaries are corrected with a  $5 \times 5$  pixel mask algorithm. In the final software run, the four restored images are searched for particles, and each particle detected is characterized by its projected area and its center of mass determined from the projected particle shapes. The combination of the images taken from two orthogonal directions then allows sufficiently exact determination of the particle volumes and the centers of mass as well as of the collision dynamics such as collision velocity, impact parameter, coefficient of restitution, and fragment size distribution.

### 3. THE LOW-DENSITY DUST AGGREGATES

The goal of our experiment, namely to investigate collisions between macroscopic (millimeter-sized) dust particles, has fundamental impact on the types of projectiles to be used. Preplanetary dust growth is believed to start with micrometer- or submicrometer-sized particles (nebula condensates and/or interstellar grains) and to proceed to larger aggregates by coagulation. It is generally assumed that sticking between particles or aggregates occurs due to interparticle surface forces (e.g., van der Waals forces) if the mutual collision velocities are low enough (Dahneke 1971). Hence, impact melting, for instance, is negligible so that such low-velocity aggregation processes preserve the nature of the particles. Thus, aggregates with clearly distinguishable constituent particles of micrometer or submicrometer sizes are expected to be the outcome of these processes.

Our search for qualified analog materials representing preplanetary aggregates led us to aggregated powders of different materials. It is a common feature of fine-grained powders that aggregates of different sizes (up to several millimeters) form by shaking a container with fine dust (Clausen and Petzow 1973). We examined several powders with two different grain size regimes  $r_0$ , namely  $r_0 = O(1 \text{ } \mu\text{m})$  and  $r_0 = O(10 \text{ nm})$ , respectively. Test experiments with different powder materials from the same grain size regime showed no principal difference in the collision

behavior, so we restricted our investigations to the following two types of aggregates:

*Zirconium silicate* ( $\text{ZrSiO}_4$ ), constituent particle size =  $(0.5^{+0.5}_{-0.3}) \mu\text{m}$  (errors are for the 90 and 10% values of the total mass vs size distribution function) and

Aerosil 200 ( $\text{SiO}_2$ ), constituent particle size =  $(12 \pm 3) \text{ nm}$  (FWHM) (Degussa 1991, Evans and King 1966).

Figure 2a shows SEM images taken from a  $\text{ZrSiO}_4$  aggregate as a whole and from a part of its surface. The typically found spherical structure as well as the relatively high porosity of the aggregate are clearly visible. In Fig. 2b, a part of an Aerosil 200 aggregate is shown with a TEM image. The 12-nm constituent particles as well as the extremely low density of the aggregate can be easily recognized. In order to determine the mean density of both types of aggregates, we performed test experiments with the experimental setup described in the previous section. We determined the mean volume of the (almost spherical) aggregates by measuring the two orthogonal projection areas  $A_1$  and  $A_2$ , taking the mean projected area  $A = (A_1 + A_2)/2$  and estimating the mean volume by  $V = 4/3 \pi (A/\pi)^{3/2} = 4/3 \pi r^3$ , in which  $r$  is the mean radius of each aggregate. Preceding each measurement, we weighed the aggregates on a precision balance. Figure 3 shows the results of these test experiments. For  $\text{ZrSiO}_4$ , we determined a size-independent density of  $\rho_a = 1.20 \text{ g cm}^{-3}$ . With the density of the constituent  $\text{ZrSiO}_4$  particles  $\rho_c = 4.56 \text{ g cm}^{-3}$ , the mean porosity results in  $p_a = 1 - \rho_a/\rho_c = 0.74$ . In case of Aerosil 200, the density of the aggregates also is not dependent on the size and has the average value of  $\rho_a = 0.059 \text{ g cm}^{-3}$ . The density of the 12-nm  $\text{SiO}_2$  particles is  $\rho_c = 2.2 \text{ g cm}^{-3}$ , so that the mean porosity of the Aerosil 200 aggregates is  $p_a = 1 - \rho_a/\rho_c = 0.97$ . As the mass determination for the aggregates using a precision balance has negligible errors, we estimate from the data point scatter (see Fig. 3) the errors for the determination of aggregate masses using the experimental images to be  $\leq 10\%$ .

#### 4. PARAMETERS OF THE EXPERIMENTS

We performed 436 collision experiments with the two aggregate materials described in the previous section in five narrow velocity ranges,

$$v_1 = 0.15\text{--}0.16 \text{ m sec}^{-1}$$

$$v_2 = 0.52\text{--}0.55 \text{ m sec}^{-1}$$

$$v_3 = 1.03\text{--}1.11 \text{ m sec}^{-1}$$

$$v_4 = 1.90\text{--}2.05 \text{ m sec}^{-1}$$

$$v_5 = 3.80\text{--}3.86 \text{ m sec}^{-1},$$

the width of these velocity windows being the intrinsic scatter between the different experimental runs.

For  $\text{ZrSiO}_4$ , we chose two different mass ratios  $m_2/m_1$  of the colliding aggregates (see Fig. 4 for the mass distributions). One series of experiments was performed with almost equal mass aggregates (in the following  $\text{ZrSiO}_4(\text{I})$ ), the mean radius of the bigger cluster being  $r_2 = 0.9 \text{ mm}$  and the mean mass ratio being  $m_2/m_1 = 1.18$ . The other experiment series was taken with maximum possible aggregate mass ratio (in the following  $\text{ZrSiO}_4(\text{II})$ ). Here, the mean radius of the bigger clusters was  $r_2 = 1.0 \text{ mm}$ , and the mean mass ratio was measured to be  $m_2/m_1 = 65.8$ . Experiments with Aerosil 200 clusters were performed with almost equal-sized aggregates only. The mean radius of the bigger clusters was  $r_2 = 1.1 \text{ mm}$ , the mean mass ratio  $m_2/m_1 = 1.28$ .

Table 1 summarizes the numbers of experiments performed for these three collision types ( $\text{ZrSiO}_4(\text{I})$ ,  $\text{ZrSiO}_4(\text{II})$ , Aerosil 200) in the five velocity ranges mentioned above. The extremely low number of collision experiments performed for Aerosil 200 in the lowest velocity range  $v_1$  results from a tremendously diminished collision probability at the lowest relative velocities.

To obtain maximum possible astrophysical relevance with our experiments, we tried to vary the impact parameters of the collisions to simulate a statistical distribution of impact parameters. In the following section, we will use the *normalized impact parameter*  $b/r = b/(r_1 + r_2)$ , with  $b$  being the ordinary impact parameter, i.e., the projection of the center-of-mass distance perpendicular to the relative velocity vector,  $r_1$  and  $r_2$  representing the mean particle radii, and  $r = r_1 + r_2$ . *Central collisions* are represented by  $b/r = 0$  and *grazing collisions between spheres* by  $b/r = 1$ . Each of the 436 experiments was characterized with respect to one of the following three results:

—*restitution*: particles bounce off after the collision without measurable mass loss or mass transfer

—*coagulation*: particles stick together after the collision

—*fragmentation*: at least one of the projectiles disintegrates into at least two parts.

In case of restitution, we also measured the so-called *coefficient of restitution*  $\epsilon$ , i.e., the ratio of the relative velocity of the projectiles after the collision to the relative velocity before the collision.  $\epsilon$  is restricted to  $0 \leq \epsilon \leq 1$ , with  $\epsilon = 0$  meaning a completely inelastic collision (coagulation) and  $\epsilon = 1$  meaning a perfect elastic collision. In the case of fragmentation, we also determined the mass of each of the fragments.

#### 5. EXPERIMENTAL RESULTS

As examples for typical  $\text{ZrSiO}_4$  aggregate collisions, Fig. 5 shows collisions at different velocities. Figure 5a

demonstrates a typical case of low-velocity restitution of equal sized aggregates. The relative velocity was  $v = 0.15 \text{ m sec}^{-1}$  (see figure caption for details). In Fig. 5b, a case of an intermediate velocity ( $v = 2.0 \text{ m sec}^{-1}$ ) restitution of different mass aggregates ( $m_2/m_1 = 113$ ) is shown, and Fig. 5c is an example for a high-velocity ( $v = 3.8 \text{ m sec}^{-1}$ ) fragmentation event of equal-sized clusters. In none of the 436 collision experiments (and also not in many more test experiments with  $\text{ZrSiO}_4$ ,  $\text{CaTiO}_3$ , and  $\text{TiO}_2$  aggregates), was coagulation, i.e., the sticking of the aggregates after the collision, observed.

The dominant process for  $\text{ZrSiO}_4(\text{I})$  collisions in the lower part of the velocity region investigated ( $v \leq 1 \text{ m sec}^{-1}$ ), and for  $\text{ZrSiO}_4(\text{II})$  and Aerosil 200 aggregate collisions in general, is restitution. For each of these bouncing collisions, we measured the coefficient of restitution  $\epsilon$  (see previous section) and the normalized impact parameter  $b/r$ . It is convenient and of physical interest to present the data in an  $\epsilon^2$  vs  $(b/r)^2$  plot,  $\epsilon^2$  meaning the fraction of translational energy remaining in the aggregates' motions after the collision, and the width of a  $(b/r)^2$  interval represents the statistic collision probability for that impact parameter interval. Figure 6 shows these data for the five velocity ranges investigated. Note that for  $\text{ZrSiO}_4(\text{I})$ , due to the strongly increasing fragmentation probability and due to a change in the observation technique (we took only one image after the collisions), the measurement of the coefficient of restitution was not possible for the two largest velocities  $v_4$  and  $v_5$ , respectively. A common feature of all plots in Fig. 6 is that, independent of material or mass ratio,  $\epsilon^2$  increases with increasing  $(b/r)^2$ ; i.e., collisions are more elastic in the case of grazing incidence compared to central collisions which are considerably less elastic. The most prominent differences for the three types of collisions investigated in this work are (1)  $\epsilon^2$  for central collisions ( $(b/r)^2 = 0$ ) is significantly higher for  $\text{ZrSiO}_4(\text{II})$  than for  $\text{ZrSiO}_4(\text{I})$  and even higher for Aerosil 200 and (2) data points scatter much more for Aerosil 200 than for  $\text{ZrSiO}_4(\text{I})$  and  $\text{ZrSiO}_4(\text{II})$ . Statistical analysis of the data plotted in Fig. 6 showed that  $\epsilon^2$  is not velocity dependent within the significance limits.

Theoretical considerations (developed in Section 6) predict a linear relation between  $\epsilon^2$  and  $(b/r)^2$  for spherical projectiles,

$$\epsilon^2 = \epsilon^2(0) + (\epsilon^2(1) - \epsilon^2(0)) \cdot (b/r)^2, \quad (2)$$

where  $\epsilon(0)$  is the coefficient of restitution for central collisions and  $\epsilon(1)$  is the coefficient of restitution for grazing collisions. We estimated the parameters  $\epsilon^2(0)$  and  $\epsilon^2(1)$  for the three types of collisions by fitting Eq. 2 to the data using the least squares method. Combining the results for the various velocities, we get the mean parameters  $\epsilon_m^2(0)$  and  $\epsilon_m^2(1)$  as well as estimations of their errors. Table II

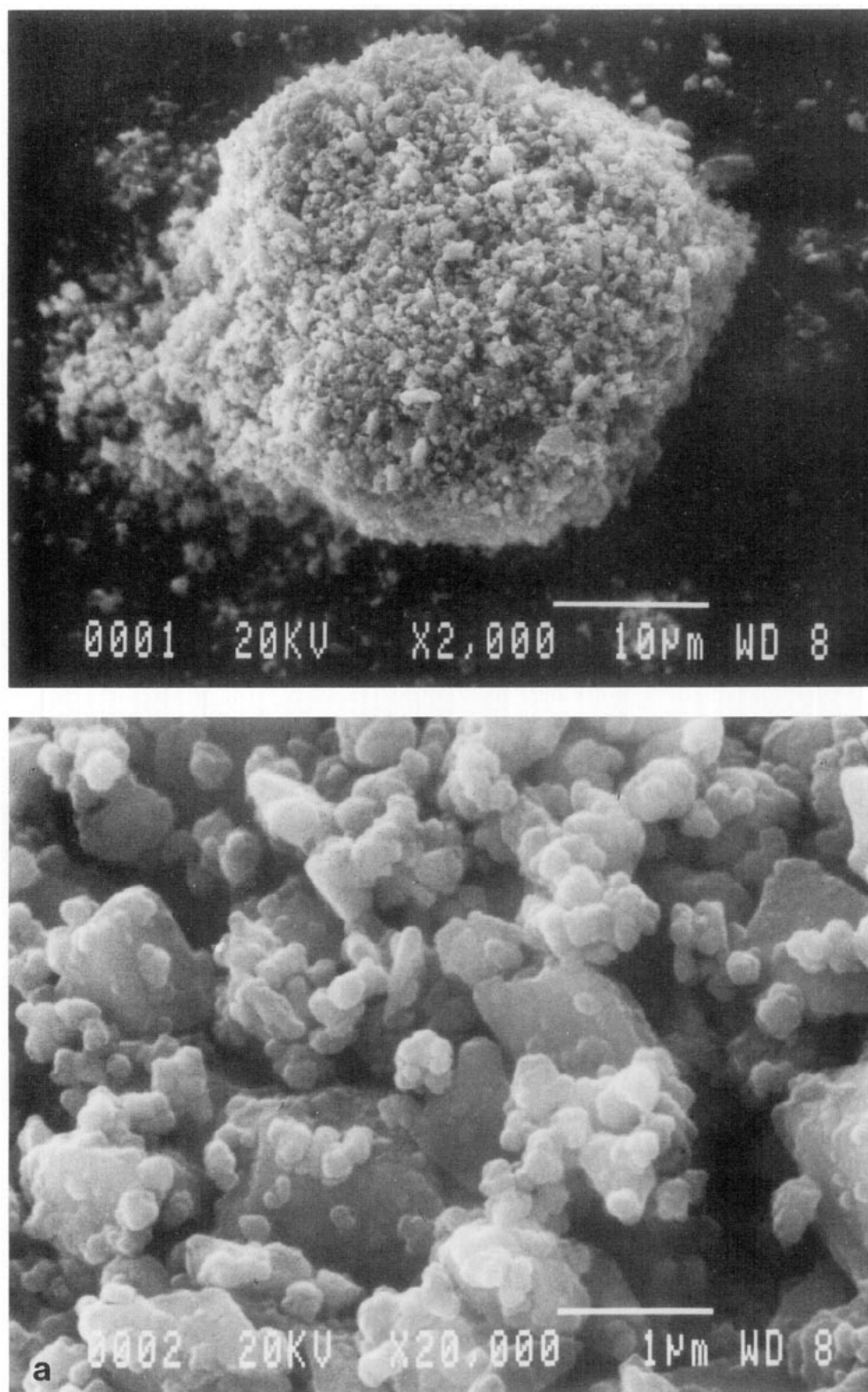
lists these results. As we mentioned above,  $\epsilon_m^2(0)$  is larger for  $\text{ZrSiO}_4(\text{II})$  than for  $\text{ZrSiO}_4(\text{I})$  but it is the largest for Aerosil 200. Within the uncertainties,  $\epsilon_m^2(1)$  does not depend on the type of collision. Although the Aerosil 200 data points scatter considerably, the systematic increase of  $\epsilon^2$  with increasing  $(b/r)^2$  is statistically significant.

Fragmentation, the break-up of aggregates during collisions, was the dominant process for  $\text{ZrSiO}_4(\text{I})$  collisions with  $v \geq 1 \text{ m sec}^{-1}$  and occurred in 26% of the collisions for  $v_3$ , 55% for  $v_4$ , and 98% for  $v_5$ . In the case of  $\text{ZrSiO}_4(\text{II})$ , only two collisions (8%) resulted in fragmentation, whereas 27% of the Aerosil 200 aggregates fragmented at  $v_5$ . For these two types of aggregates, fragmentation was not observed for lower velocities. As a measure of the strength of fragmentation, we define the mass loss  $\mu$ ,

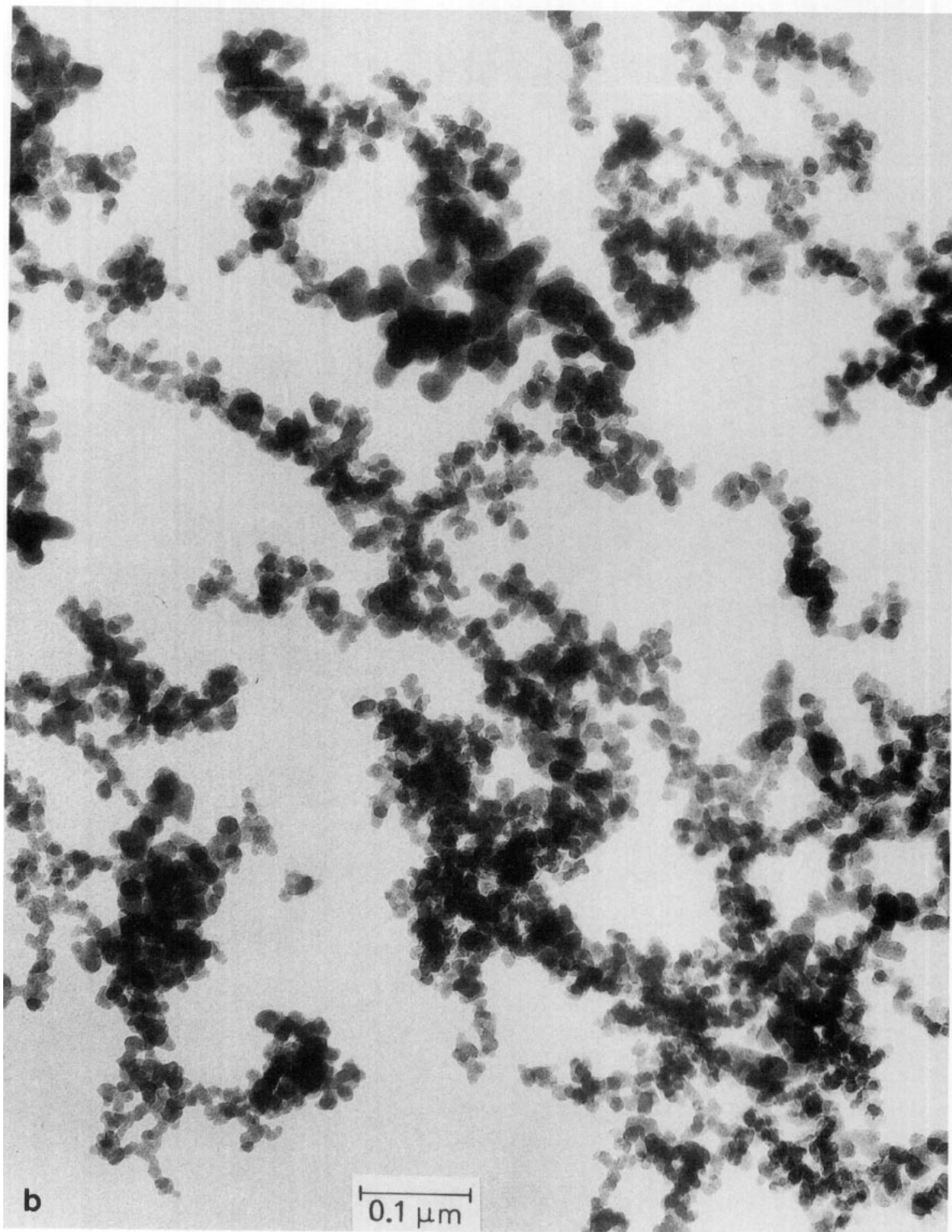
$$\mu = \frac{\text{total mass of all fragments} - \text{except the two largest fragments}}{\text{total mass of all fragments}}, \quad (3)$$

$\mu = 0$  meaning collisions without fragmentation,  $\mu \rightarrow 1$  meaning complete destructive fragmentation, i.e., the disintegration of the aggregates into their constituent solid particles. To simplify matters, we present here only our statistical analysis of the mass losses for the  $\text{ZrSiO}_4(\text{I})$  collisions. We sampled all mass loss data (including the restitution cases with  $\mu = 0$  to get a statistically relevant sample) into the four  $(b/r)^2$  intervals,  $0 \leq (b/r)^2 < 0.25$ ,  $0.25 \leq (b/r)^2 < 0.50$ ,  $0.50 \leq (b/r)^2 < 0.75$ , and  $0.75 \leq (b/r)^2$ , and took the arithmetic mean of the measured  $(b/r)^2$  and  $\mu$  values (see Fig. 7). The error bars in Fig. 7 indicate the variances of the mean  $(b/r)^2$  and  $\mu$  values within the intervals. Two prominent facts can be seen from Fig. 7: (1)  $\mu$  strongly increases with increasing collision velocity above  $v \approx 1 \text{ m sec}^{-1}$  and (2)  $\mu$  increases with decreasing normalized impact parameter; i.e., central collisions lead to stronger mass losses than grazing incidences. Even for  $v_5$ , the mass losses are in the percentage range for glancing incidences. For  $(b/r)^2 = 0.5$ , the mean relative impact parameter for spherical projectiles, we estimated mass losses of  $\mu = 1\%$  at  $v_3$ ,  $\mu = 8\%$  at  $v_4$ ,  $\mu = 29\%$  at  $v_5$  for  $\text{ZrSiO}_4(\text{I})$ , and  $\mu = 3\%$  at  $v_5$  for Aerosil 200.

Along with the mass losses, we also recorded the masses of the resulting fragments and derived their mass distribution. We sampled the fragment masses into logarithmic mass intervals centered at  $\frac{1}{2}$ ,  $\frac{1}{4}$ ,  $\frac{1}{8}$ , . . . of the mean total mass of the two colliding projectiles (original aggregates have, in this definition, masses of  $\sim \frac{1}{2}$  the total mass), and we derived the total mass fraction of fragments in these individual fragment mass bins. We normalized the total mass fractions so that their sum is unity. Figure 8 shows these results, Fig. 8a for  $\text{ZrSiO}_4(\text{I})$  and  $v_3$ ,  $v_4$ ,



**FIG. 2.** (a) SEM micrographs of a  $\text{ZrSiO}_4$  aggregate: (top) 40- $\mu\text{m}$  aggregate (scale bar 10  $\mu\text{m}$ ), (bottom) surface of an aggregate with the constituent particles (scale bar 1  $\mu\text{m}$ ). (b) TEM image of an Aerosil 200 aggregate. By courtesy of Degussa AG, Frankfurt, Germany.

**FIG. 2—Continued**



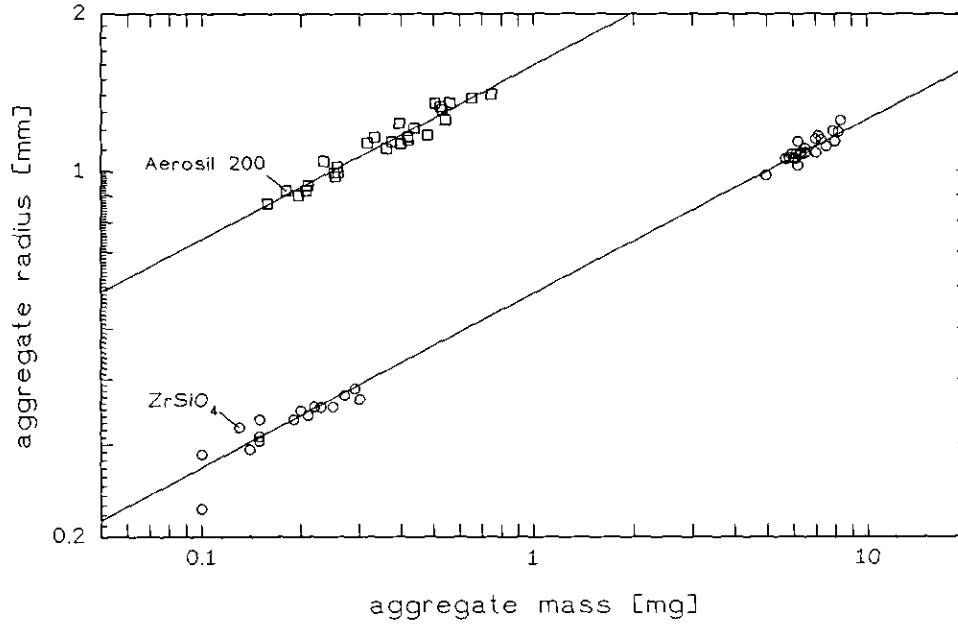


**FIG. 3.** Density determination of the  $\text{ZrSiO}_4$  and Aerosil 200 aggregates. Aggregates were weighed with a precision balance prior to the experiments and their mean radii were measured from the CCD images (see text). The solid lines represent the constant aggregate densities of  $\rho_a = 1.20 \text{ g cm}^{-3}$  for  $\text{ZrSiO}_4$  and  $\rho_b = 0.059 \text{ g cm}^{-3}$  for Aerosil 200.

and  $v_5$  and Fig. 8b for Aerosil 200 and  $v_5$ . Due to limited camera resolution, we could not detect fragments with fragment mass/total mass  $\leq 2 \times 10^{-4}$ . With increasing collision velocity the relative importance of the fragments with masses smaller than the original aggregate masses increases steeply. The fragment mass distribution for  $\text{ZrSiO}_4(\text{I})$  at  $v_5$  follows approximately the power law  $M_i \sim m_i^\lambda$ , with  $M_i$  being the total mass fraction of the fragments in the mass bin centered around the mass  $m_i$  and  $\lambda \approx \frac{7}{8}$ . The Aerosil 200 fragment mass distribution for  $v_5$  is somewhat steeper compared to that for  $\text{ZrSiO}_4(\text{I})$  and is truncated at the relative fragment masses  $< 10^{-2}$ ; i.e., fragments with relative masses  $< 10^{-2}$  were not detected. We see that for  $\text{ZrSiO}_4(\text{I})$ , the overall mass loss increases and small fragments become more important with increasing velocity. For Aerosil 200, the total mass loss is smaller compared to  $\text{ZrSiO}_4(\text{I})$  and is dominated by large fragments similar to  $\text{ZrSiO}_4(\text{I})$  at smaller velocities.

## 6. INTERPRETATION OF THE RESULTS

In this section, we derive the linear dependence (that has been used when fitting Eq. (2) to the data points in Fig. 6) of the normalized translational energy after the collision  $\epsilon^2$  on the squared normalized impact parameter  $(b/r)^2$ . We start by decomposing the collision of the two projectiles into a *normal* and a *tangential* component. We define the velocity-independent normal and tangential coefficients of restitution  $\epsilon_n$  and  $\epsilon_t$ , respectively, by

$$\epsilon_n = \frac{v'_n}{v_n} \quad (4)$$

and

$$\epsilon_t = \frac{v'_t}{v_t}, \quad (5)$$

with

$$v_t'^2 + v_n'^2 = v'^2 \quad (6)$$

and

$$v_t^2 + v_n^2 = v^2. \quad (7)$$

$v$  and  $v'$  are the relative velocities before and after the collision,  $v_n$  and  $v_t$  are the normal and tangential components of the relative velocity before the collision, and  $v'_n$  and  $v'_t$  are those of the relative velocity after the collision. These components are related to the total relative velocities by

$$v_n^2 = (1 - (b/r)^2)v^2 \quad (8)$$

and



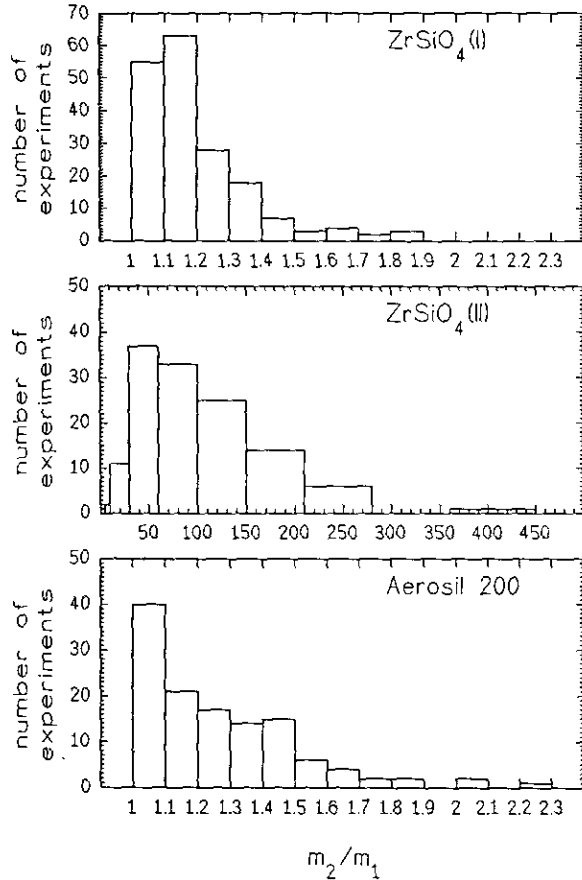


FIG. 4. Distribution of mass ratios  $m_2/m_1$  of the two colliding aggregates with the masses  $m_2$  and  $m_1 \leq m_2$  for the three types of collisions investigated.

$$v_t^2 = (b/r)^2 v^2. \quad (9)$$

With the definition of the coefficient of restitution

$$\varepsilon = \frac{v'}{v} \quad (10)$$

and Eqs. (4)–(9), we can easily derive Eq. (2) with  $\varepsilon^2(0) =$

$\varepsilon_n^2$  and  $\varepsilon^2(1) = \varepsilon_t^2$ . This is just the type of observed linear dependence of the normalized kinetic energy after the collision  $\varepsilon^2$  on the squared normalized impact parameter  $(b/r)^2$ .

In this connection,  $\varepsilon_n^2$  is due to plastic flow effects (like reorganization of constituent particles or compaction of a part of the aggregate). Johnson (1985) derives an expression for the central coefficient of restitution of solid spheres, which we adopt here for the normal component of  $\varepsilon^2$  as

$$\varepsilon_n^2 \approx 13.7 \left( \frac{Y_d}{E^*} \right) \left( \frac{\frac{1}{2} m v_n^2}{Y_d R^3} \right)^{-1/4}, \quad (11)$$

where  $Y_d$  denotes the dynamic yield strength of the weakest of the two (solid) materials,  $E^*$  is related to the Young's moduli  $E_1$  and  $E_2$  and to the Poisson numbers  $\sigma_1$  and  $\sigma_2$  of the two colliding spheres by  $(E^*)^{-1} = (1 - \sigma_1^2)/E_1 + (1 - \sigma_2^2)/E_2$ ,  $m^{-1} = m_1^{-1} + m_2^{-1}$  defines the reduced mass  $m$  of the two spheres with the masses  $m_1$  and  $m_2$  and the radii  $r_1$  and  $r_2$ , respectively. The reduced radius is defined by  $R^{-1} = r_1^{-1} + r_2^{-1}$ . The basis of the validity of Eq. (11) is (see Johnson 1985) (1) irreversible plastic creep of the weakest of the colliding bodies if the contact pressure  $p_0$  exceeds the yield strength of the material, (2) the dynamic impact pressure  $p_d$  is limited to  $p_d \approx 3 \cdot Y_d$ , and (3) the rebound phase is elastic.

It is unknown if Eq. (11) is applicable to the collision of weak aggregates, but nevertheless some interesting aspects in Eq. (11) may be valid for the further discussion: (1)  $\varepsilon_n^2$  is only weakly velocity dependent,  $\varepsilon_n^2 \sim v_n^{-1/2}$ . This point may explain why we could not detect any velocity dependence in our  $\varepsilon_m^2(0)$  data (see previous section). Thus, the velocity dependence may be hidden in the data point scatter. (2) For aggregates with equal materials and compositions,  $\varepsilon_n^2$  depends on the size ratio of the aggregates due to  $\varepsilon_n^2 \sim (m/R^3)^{-1/4}$ , which yields somewhat higher values for unequal masses compared to equal-sized projectiles. This may explain the higher  $\varepsilon_m^2(0)$  values for ZrSiO<sub>4</sub>(II) than for ZrSiO<sub>4</sub>(I).

For the derivation of  $\varepsilon_t^2$ , we assume that the colliding aggregates have rough surfaces, so that sliding during the collision is not possible. For the surface rotation velocities  $v'_{r,1}$  and  $v'_{r,2}$  of the spherical aggregates after the collision, this assumption yields

$$v'_{r,1} + v'_{r,2} = v'_t = \varepsilon_t v_t = \varepsilon_t (b/r) v. \quad (12)$$

The aggregates were assumed to be nonrotating before the collision as it was the case in our experimental studies. Conservation of total angular momentum gives

$$m v r (b/r) = m v' r (b'/r) + \frac{2}{5} m_1 r_1 v'_{r,1} + \frac{2}{5} m_2 r_2 v'_{r,2} \quad (13)$$

TABLE I  
Numbers of Experiments for the Three Different Collision Types (ZrSiO<sub>4</sub>(I), ZrSiO<sub>4</sub>(II), Aerosil 200) Carried Out in the Five Velocity Regimes ( $v_1, \dots, v_5$ )

	$v_1$	$v_2$	$v_3$	$v_4$	$v_5$
ZrSiO <sub>4</sub> (I)	29	26	34	49 <sup>a</sup>	45 <sup>a</sup>
ZrSiO <sub>4</sub> (II)	23	20	30	32	24
Aerosil 200	3	23	32	36	30

<sup>a</sup> Performed with a three-image technique so that the determination of the restitution coefficient for the nonfragmented aggregates was not possible.

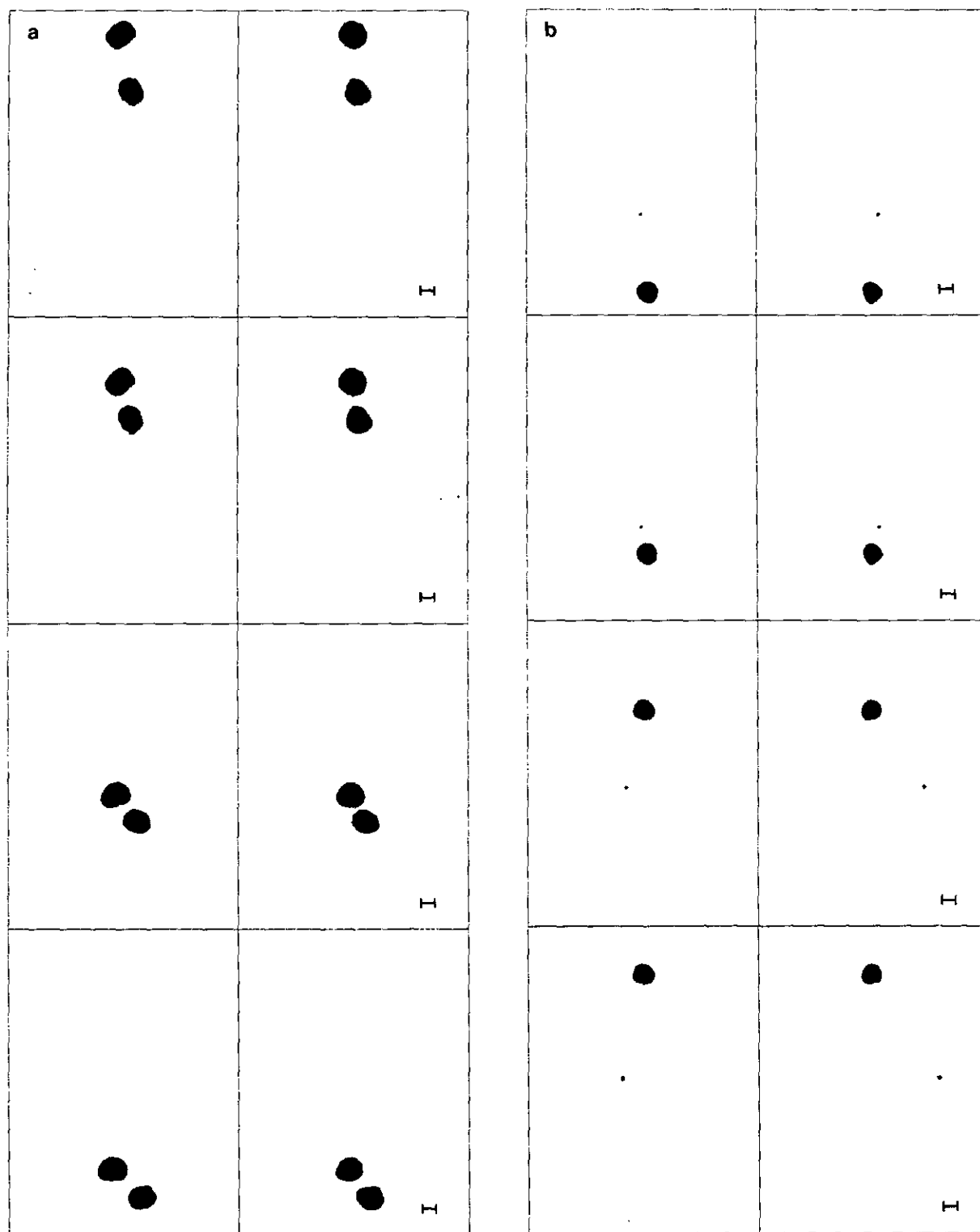


**FIG. 5.** Typical examples for  $\text{ZrSiO}_4$  aggregate collisions showing four three subsequent images taken with the CCD camera from two orthogonal directions. The bar in the lower right corner shows a scale of 1 mm. (a) A low-velocity  $\text{ZrSiO}_4(\text{I})$  collision ( $v = 0.15 \text{ m sec}^{-1}$ ,  $b/r = 0.53$ ) resulting in restitution. Image times were (from top to bottom):  $T_1 = 90 \text{ msec}$ ,  $T_2 = 100 \text{ msec}$ ,  $T_3 = 120 \text{ msec}$ ,  $T_4 = 130 \text{ msec}$ . (b) An intermediate velocity  $\text{ZrSiO}_4(\text{II})$  collision ( $v = 2.0 \text{ m sec}^{-1}$ ,  $b/r = 0.73$ ) resulting in restitution.  $T_1 = 10 \text{ msec}$ ,  $T_2 = 12 \text{ msec}$ ,  $T_3 = 19 \text{ msec}$ ,  $T_4 = 21 \text{ msec}$ . (c) A high-velocity  $\text{ZrSiO}_4(\text{I})$  collision ( $v = 3.8 \text{ m sec}^{-1}$ ,  $b/r = 0.49$ ) resulting in fragmentation. Note that image 4 was omitted.  $T_1 = 7.2 \text{ msec}$ ,  $T_2 = 8.0 \text{ msec}$ ,  $T_3 = 14.0 \text{ msec}$ .

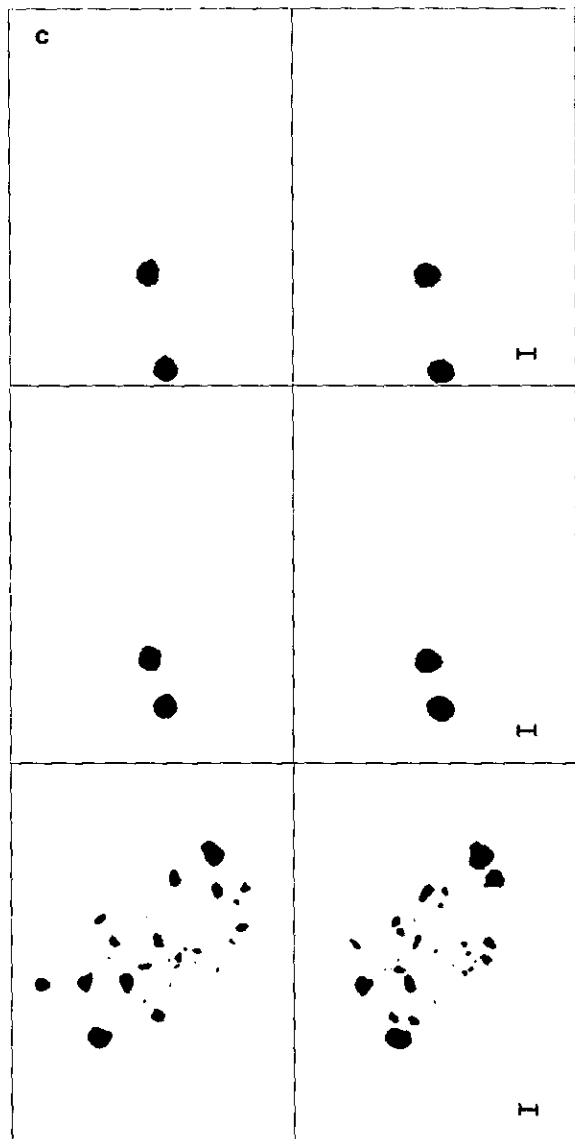


FIG. 5—Continued

with  $r = r_1 + r_2$ , assuming homogeneous spherical aggregates.  $b'/r$  is the normalized rebound parameter (i.e., impact parameter after the collision) which is related to  $b/r$  by

$$v'(b'/r) = v(b/r)\epsilon_c. \quad (14)$$

As both aggregates experience the same impact force, the following relation is valid:

$$v'_{r,1}/v'_{r,2} = m_2/m_1. \quad (15)$$

With the scaling relations

$$r_2 = \alpha r_1 \quad (16)$$

and

$$m_2 = \alpha^3 m_1, \quad (17)$$

assuming equal densities for the two colliding bodies, and with some algebra, we can derive

$$\epsilon_1^2 = \left(\frac{2}{3}\right)^2 \approx 0.510, \quad (18)$$

which is independent of the radii ratio  $\alpha$ .

Equation (18) does not violate energy conservation as the gain of rotation energy  $\Delta E_{\text{rot}}$  is always smaller than the loss of (linear) kinetic energy  $\Delta E_{\text{kin}}$ :

$$\Delta E_{\text{rot}} \leq \Delta E_{\text{kin}}. \quad (19)$$

Inequality (19) expresses the need for some kind of irreversible energy dissipation even for grazing collisions. The comparison of the calculated value  $\epsilon_1^2 \approx 0.510$  with the measured data of  $\epsilon_m^2(1)$  (see Table II) shows that both results are in good agreement so that the a priori assumption that no sliding of the contacting surfaces occurs is justified.

#### 7. COMPARISON WITH OTHER EXPERIMENTS AND PREDICTIONS FOR THE OUTCOME OF COLLISIONS BETWEEN AGGREGATES AT DIFFERENT VELOCITIES

Impact or collision experiments using powder or aggregate projectiles and/or targets were also performed by Hartmann (1978) and Ryan *et al.* (1991). Hartmann (1978) performed drop experiments of centimeter-scale dirt clod projectiles (aggregates) onto flat rock targets. He found the transition velocity between rebound and catastrophic fragmentation (defined by largest fragment equaling half original mass) to be  $\sim 2 \text{ m sec}^{-1}$  and the fragmentation onset to be  $\sim 0.5 \text{ m sec}^{-1}$ . Ryan *et al.* (1991) performed (among other types of experiments) drop tests of glued aggregates onto concrete targets and onto basalt powder. Their aggregate sizes are in the centimeter range. They find the rebound-fragmentation transition velocity to be  $\sim 7 \text{ m sec}^{-1}$  and the fragmentation onset velocity to be  $\sim 1 \text{ m sec}^{-1}$ .

It is difficult to compare these results with ours because (1) the above-cited experiments represent central collisions ( $b/r = 0$ ), (2) the constituent particle sizes of the aggregates used in the different experiments were not specified and may be different from ours and presumably much larger, and (3) aggregate sizes were approximately 10 times larger than those used in our experiments.

The onset of fragmentation in our experiments was observed for collision velocities of  $\sim 1 \text{ m sec}^{-1}$ , the transition

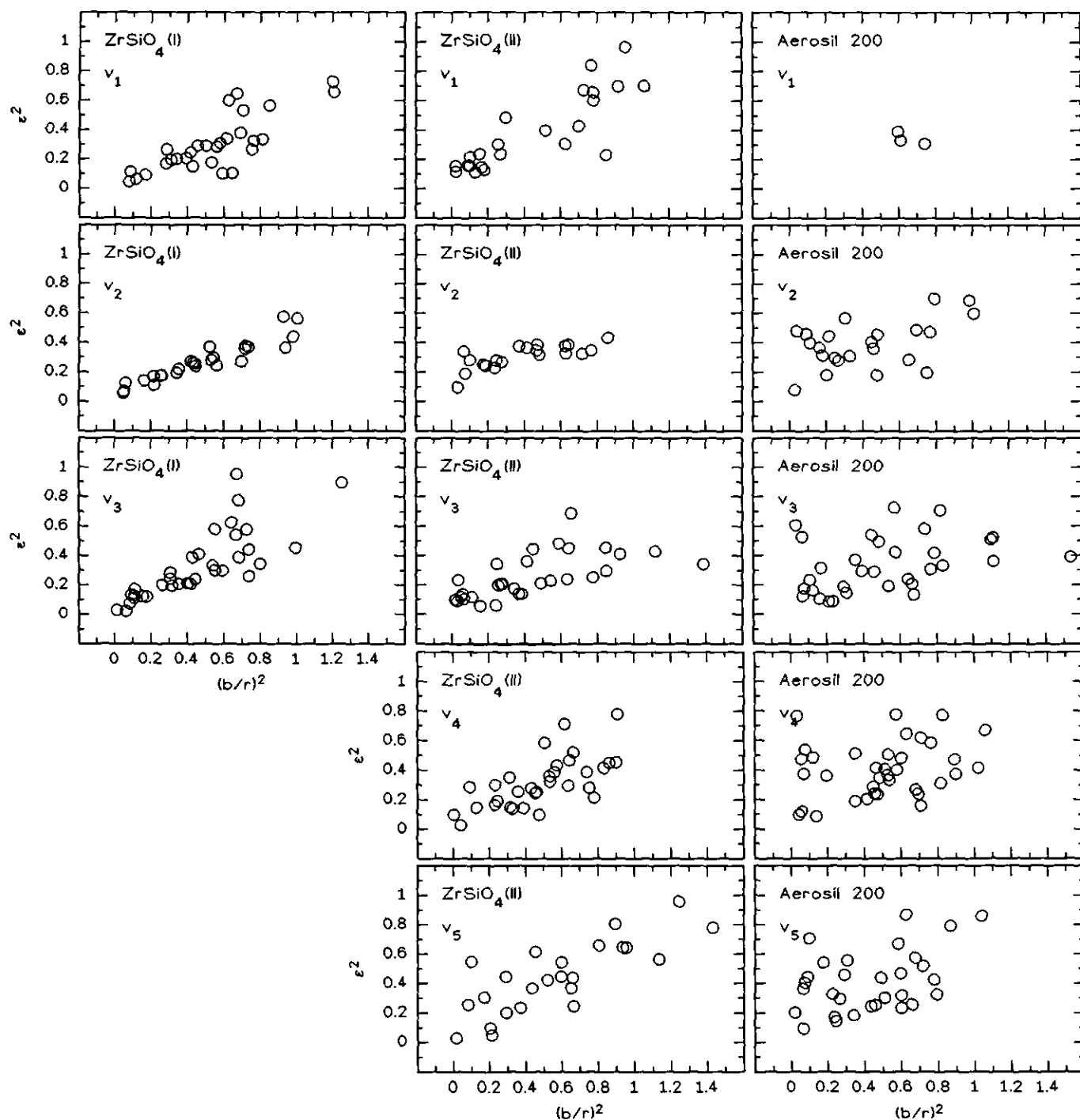


FIG. 6. Dependence of the normalized translational energy  $\epsilon^2$  on the squared normalized impact parameter  $(b/r)^2$  for the experiments with  $\text{ZrSiO}_4(\text{I})$ ,  $\text{ZrSiO}_4(\text{II})$ , and Aerosil 200 in the five velocity regimes  $v_1, \dots, v_5$ .

velocity between rebound and catastrophic fragmentation (in the above definition) for central collisions is  $\sim 4 \text{ m sec}^{-1}$ .

In this section, we derive a simple theoretical model of

the dependence of a power-law fragment mass distribution on the collision velocity. With this model and with assumptions about the binding energies of the constituent particles inside an aggregate, we will make predictions

TABLE II

The Mean Squared Restitution Coefficients for Normal Incidence,  $\varepsilon_m^2(0)$ , as well as for Grazing Incidence,  $\varepsilon_m^2(1)$ , for the Three Collision Types Investigated

	$\varepsilon_m^2(0)$	$\varepsilon_m^2(1)$
ZrSiO <sub>4</sub> (I)	0.040 ± 0.025	0.572 ± 0.070
ZrSiO <sub>4</sub> (II)	0.127 ± 0.022	0.575 ± 0.061
Aerosil 200	0.289 ± 0.029	0.496 ± 0.081

on the fragmentational outcome of low-velocity collisions of preplanetary dust aggregates.

Aggregates that consist of loosely bonded constituent particles have free surface energies  $E_s$  due to unsaturated particle-particle bonds at the aggregate surfaces. To reach fragmentation, the excess free surface energy of the fragments has to be provided by a part of the impact energy

$$\sum_i E_s^i(\text{after}) - \sum_j E_s^j(\text{before}) = \frac{1}{2}\beta\mu v^2, \quad (20)$$

where the first summation on the left-hand side of Eq. (20) runs over all fragments  $i$ , and the second summation runs over the two original colliding aggregates ( $j = 1, 2$ ), respectively;  $\mu$  is the reduced mass and  $\beta$  indicates an efficiency parameter for the energy transfer into fragmentation energy. From the theoretical considerations in Section 6 it can be deduced that the statistical mean value for  $\beta$  (i.e., the value for an impact parameter  $(b/r)^2 = 0.5$ )

is  $\beta = (1 - \varepsilon_n^2)(1 - (b/r)^2)$  and lies in the range  $0 \leq \beta \leq 0.5$ .

In the following, we assume that both colliding aggregates have the same mass  $m$  and that the fragments follow the power law mass distribution

$$\nu(m') dm' = \nu_0 m'^k dm' \quad (21)$$

in the mass range from  $m_0$  (constituent particle mass) to  $m$  (original aggregate mass), in which  $\nu(m') dm'$  is the number of fragments in the mass range between  $m'$  and  $m' + dm'$ .

Mass conservation requires

$$\int_{m_0}^m \nu(m') m' dm' = 2m, \quad (22)$$

and with Eq. (21), we can deduce

$$\frac{\nu_0}{k+2} [m^{k+2} - m_0^{k+2}] = 2m. \quad (23)$$

Equation (20) can be rewritten as

$$\frac{E}{\Delta A} = \frac{\frac{1}{2}\beta\mu v^2}{A(\text{after}) - A(\text{before})}, \quad (24)$$

where  $E/\Delta A$  means the specific surface enhancement energy and  $A(\text{after})$  and  $A(\text{before})$  denote the total outer surface of the fragments and the original aggregates, re-

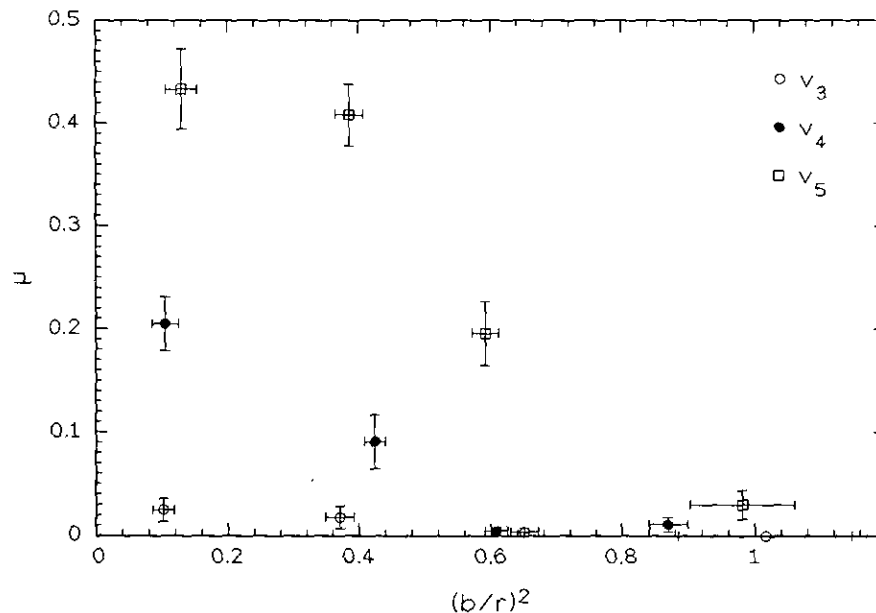
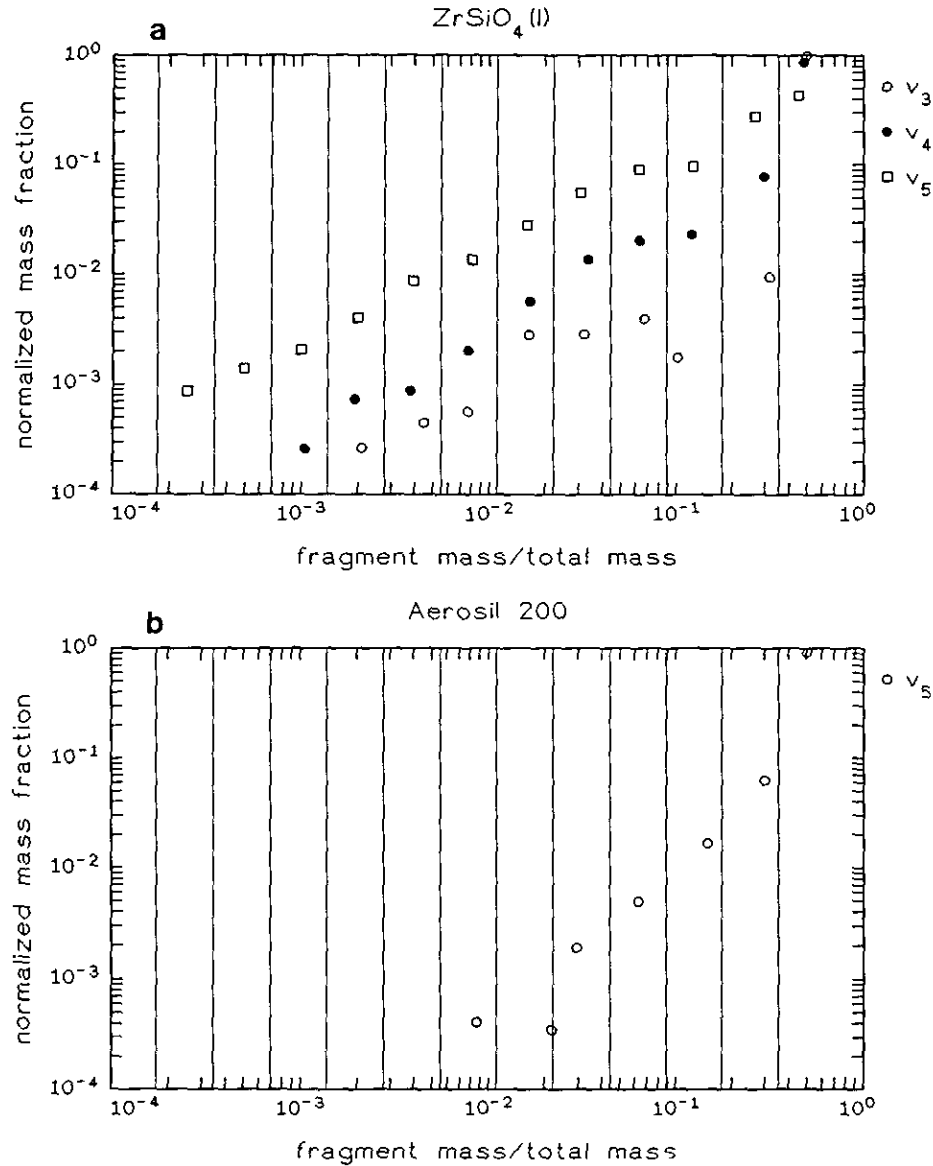


FIG. 7. Dependence of the mass loss  $\mu$  (see text for definition) on the squared normalized impact parameter  $(b/r)^2$  for ZrSiO<sub>4</sub>(I) and three different velocities  $v_3$ ,  $v_4$ , and  $v_5$ .



**FIG. 8.** Distribution of fragment masses. On the vertical axis, the normalized mass fraction of fragments within mass bins of factor 2 width (between the vertical solid lines) is shown. The horizontal axis denotes the ratio of fragment mass to the total mass of the two colliding grains before the collision. The sum of all normalized fragment mass fractions for any collision type is unity. (a)  $\text{ZrSiO}_4(\text{I})$ . (b) Aerosil 200.

spectively. With the power law fragment mass distribution, Eq. (24) can be transformed to

$$\frac{E}{\Delta A} = \frac{\frac{1}{4}\beta m^{1/3} v^2 c}{\frac{k+2}{k+\frac{5}{3}} (m/m_0)^{1/3} \left\{ \frac{(m/m_0)^{k+5/3} - 1}{(m/m_0)^{k+2} - 1} \right\} - 1}, \quad (25)$$

with  $c = (8\pi(\frac{3}{4}\pi\rho)^{2/3})^{-1}$  and  $\rho$  as the mass density of the aggregates.

In Fig. 9a, we have plotted the power index  $k$  as a function of the collision velocity for three different spe-

cific surface enhancement energies  $E/\Delta A = 0.1, 1, 10 \text{ J m}^{-2}$ . As  $\varepsilon_n^2 \approx 0$  for  $\text{ZrSiO}_4(\text{I})$ , we get  $\beta = 0.5$  basing on the above discussion. We have added the measured slope of the fragment mass distribution for  $\text{ZrSiO}_4(\text{I})$  at  $v_5$ ,  $k = -\frac{9}{8}$ . Additionally, we have plotted the two horizontal lines  $k = -\frac{5}{3}$  and  $k = -2$ , below which the small fragments dominate in surface area and mass, respectively.

From Fig. 9a, we can see that for our  $\text{ZrSiO}_4$  aggregates the typical surface enhancement energy is  $E/\Delta A \approx 0.5 \text{ J m}^{-2}$ .

At the moment, we treat  $E/\Delta A$  as a free parameter whose estimation for preplanetary dust particles will fol-

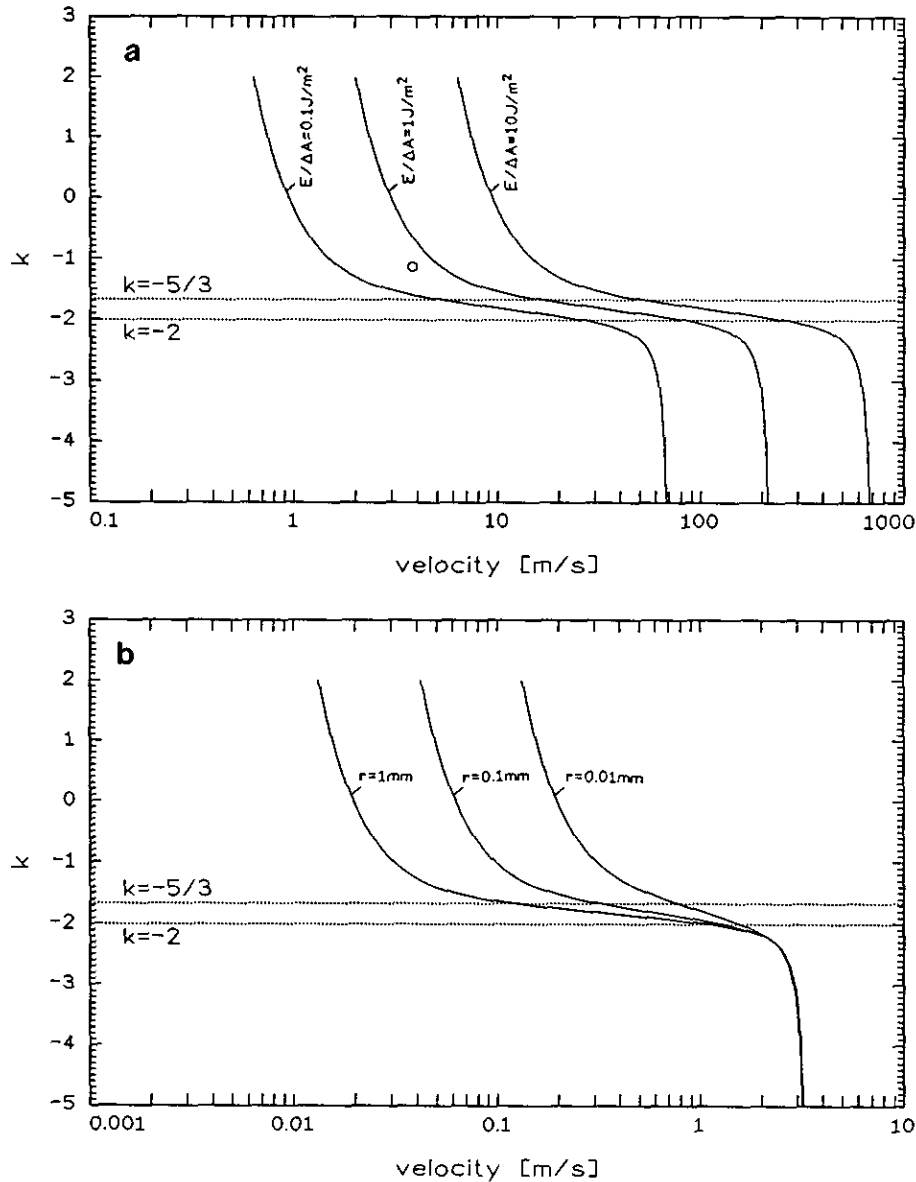


**FIG. 9.** Dependence of the power index  $k$  of the calculated power law fragment mass distribution  $\nu(m) dm = \nu_0 m^k dm$  on the collision velocity for the assumed squared impact parameter  $(b/r)^2 = 0.5$  and equal sized spherical aggregates (solid curves). The dotted horizontal lines denote boundary values for  $k$  below which the smallest aggregates (or constituent particles) dominate in cross section ( $k = -5/3$ ) and mass ( $k = -2$ ), respectively. (a) For different surface enhancement energies  $E/\Delta A = 0.1, 1, 10 \text{ J m}^{-2}$  of a representative  $\text{ZrSiO}_4(\text{I})$  collision with  $m = 3.7 \times 10^{-6} \text{ kg}$  and  $m_0 = 2.4 \times 10^{-15} \text{ kg}$ . The data point corresponds to the  $\text{ZrSiO}_4(\text{I})$  fragmentation at  $v_5$ . (b) for van der Waals bonded aggregates with the constituent particle radius  $r_0 = 0.1 \mu\text{m}$  and the aggregate radii  $r = 0.01, 0.1, 1 \text{ mm}$  (see text for details).

low afterward. From Eq. (25) and Fig. 9a, we see that for a given  $k$  the velocity scales as  $v \sim (E/\Delta A)^{1/2}$ . For  $E/\Delta A = 0.5 \text{ J m}^{-2}$ , the small fragments will dominate in cross section (i.e.,  $k < -5/3$ ) for  $v > 10 \text{ m sec}^{-1}$  and in mass (i.e.,  $k < -2$ ) for  $v > 50 \text{ m sec}^{-1}$ .

However,  $E/\Delta A$  depends on many parameters such as (a) aggregate porosities, (b) constituent particle sizes, and (c) binding energies of the constituent particles. We be-

lieve that for very porous aggregates and extremely weakly bonded constituent particles, as is assumed to be the case for preplanetary dust aggregates,  $E/\Delta A$  can be much smaller than  $1 \text{ J m}^{-2}$ , so that, even for collisions in the meters per second range, fragment mass distributions that are dominated in mass by small particles (i.e.,  $k \approx -2$ ) can result. In the following, we estimate the surface enhancement energy with a simple model and on the fol-



lowing assumptions: (1) aggregates are homogeneous in density, (2) the difference in *number of next neighbors* for constituent particles inside the aggregate and at the surface is  $\Delta n = 1$ , (3) the particle–particle binding energy is given by a sphere–sphere van der Waals contact energy  $E_0 = Ar_0/(12z_0)$  (Dahneke 1971, 1972, and references therein), where  $A \approx 10^{-19}$  J is the van der Waals constant,  $r_0$  is the constituent particle radius, and  $z_0 \approx 4 \times 10^{-10}$  m is the equilibrium distance between the two contacting surfaces, (4) the number of surface particles  $N_s$  inside a surface shell of depth  $\tau = 2r_0$  is given by  $N_s = 4\pi r^2 \tau \rho / m_0$  in which  $r$  is the aggregate radius,  $\rho$  the mass density of the aggregate, and  $m_0$  the mass of the constituent particles.

Then  $E/\Delta A$  can be expressed by

$$\frac{E}{\Delta A} = \frac{N_s E_0 \Delta n}{4\pi r^2} = \frac{\tau \rho A r_0}{12 m_0 z_0}. \quad (26)$$

For  $r_0 = 0.1 \mu\text{m}$ ,  $\rho = 500 \text{ kg m}^{-3}$  (i.e., porosity 0.8), and  $m_0 = 10^{-17} \text{ kg}$ , we get  $E/\Delta A = 2 \times 10^{-5} \text{ J m}^{-2}$  for the surface enhancement energy. Figure 9b shows the  $k$ – $v$  plot for this value. The three curves represent aggregates with radii of 1, 0.1, and 0.01 mm, respectively. The onset of fragmentation starts at lower velocities for the bigger aggregates. This fact is supported by our experimental results for the  $\text{ZrSiO}_4(\text{I})$  and  $\text{ZrSiO}_4(\text{II})$  fragmentations. Complete disintegration of the aggregates into their constituent particles ( $k \ll -2$ ) does not depend of the aggregate size and is reached for collision velocities of  $\sim 3 \text{ m sec}^{-1}$ .

## 8. CONCLUSIONS

In the preceding sections, we have experimentally shown that collisions between millimeter-sized fragile aggregates do not result in sticking for the velocities investigated (i.e.,  $v \gtrsim 0.1 \text{ m sec}^{-1}$ ). A common feature of the higher-velocity collisions (i.e.,  $v \gtrsim 1 \text{ m sec}^{-1}$ ) is the occurrence of fragmentation. We have seen that in the case of  $\text{ZrSiO}_4(\text{I})$ , in which we could observe fragmentation events for three different velocities, the fragmentation probability as well as the abundance of smaller fragments become larger with increasing collision velocity. The latter fact can be described with a simple fragmentation model on the assumptions that (1) the fragment mass distribution follows a power law, as experimentally observed, (2) the potential energy on the fragments is due to their enhanced surface, and that this surface energy per unit area is constant, and (3) the proportion of collision energy that is consumed for producing aggregates can be described by  $\beta = (1 - \varepsilon_a^2) \cdot (1 - (b/r)^2)$ . With this model, predictions on the fragmentational outcome for different collision velocities and particle–particle binding energies are possible. For an aggregate with constituent particle

radii of  $r_0 = 0.1 \mu\text{m}$  and on the assumption of van der Waals contacts between the solids, we calculated a complete disintegration velocity of  $\sim 3 \text{ m sec}^{-1}$ . Above this collision velocity, the equal-sized aggregates are fragmented into their constituents.

Collisions between such  $0.1\text{-}\mu\text{m}$ -sized particles and aggregates result in sticking if the collision velocity is smaller than a critical velocity  $v_0$  given by

$$v_0 \approx \sqrt{(2E_0\beta_0/(1 - \beta_0)m_0)} \quad (27)$$

(Dahneke 1971), with  $E_0$  and  $m_0$  being the van der Waals binding energy of the constituent particles and their masses, respectively.  $\beta_0$  is a factor describing the elasticity of the collision. To simplify matters, we adopt  $\beta_0 = 0.5$  as an estimation for the elasticity of a solid–solid collision. For the above-described particles and aggregates, Eq. (27) yields  $v_0 \approx 0.6 \text{ m sec}^{-1}$ . This means that collisions between single submicrometer particles and any aggregate result in coagulation if the collision velocity is smaller than about  $1 \text{ m sec}^{-1}$  (or a little above if a second or a third collision with the same aggregate is possible after a first nonsticky collision). On the other hand, collisions between aggregates with velocities of the same order of magnitude result in complete disintegration of the colliding clusters. This is the basis of a *coagulation–fragmentation scenario* which describes the net growth of aggregates in the turbulent preplanetary nebula by a combination of fragmentation and coagulation processes (Markiewicz and Blum 1993). In this model, it is assumed that aggregate–aggregate collisions lead to complete disintegration of the aggregates into their constituent particles (i.e.,  $k < -2$ ; cf. Fig. 9b). These fragmentations are, thus, sources for small particles which can, in due course, collide with (nondestroyed) aggregates and coalesce with them. The characteristics of this scenario are that (a) a considerable and asymptotically constant fraction of the total dust mass is contained in the growing aggregates, (b) the masses of the biggest aggregates have an asymptotic time behavior  $m \sim t^6$ , and (c) the time scale for the aggregate growth is comparable to the time scale calculated by Mizuno *et al.* (1988).

## ACKNOWLEDGMENTS

We thank A. Schneider for carefully reading the manuscript. This work was supported by the Deutsche Forschungsgemeinschaft under Grant Ig 3/13-4.

## REFERENCES

- BLUM, J. 1990. Coagulation of protoplanetary dust. *Proceedings of the 24th ESLAB Symposium on the Formation of Stars and Planets, and the Evolution of the Solar System*, Friedrichshafen, 17–19 September 1990 (ESA SP-315), pp. 87–92.

- CABOT, W., V. M. CANUTO, O. HUBICKY, AND J. B. POLLACK 1987. The role of turbulent convection in the primitive solar nebula. I. Theory. *Icarus* **69**, 387-422. II. Results. *Icarus* **69**, 423-457.
- CLAUSEN, N., AND G. PETZOW 1973. Kugelherstellung durch Pulveragglomeration. *Zeitschrift für Werkstofftechnik/J. Mater. Technol.* **4**, Jahrgang, Heft 3, 148-156.
- DAHNEKE, B. 1971. The capture of aerosol particles by surfaces. *J. Colloid Interface Sci.* **37**, 342-353.
- DAHNEKE, B. 1972. The influence of flattening on the adhesion of particles. *J. Colloid Interface Sci.* **40**, 1-13.
- DEGUSSA 1991. Grundlagen von AEROSIL, *Schriftenreihe Pigmente*, No. 11. Degussa AG.
- DONN, B., AND P. MEAKIN 1989. Collisions of macroscopic fluffy aggregates in the primordial solar nebula and the formation of planetesimals. *Proc. Lunar Planet. Sci. Conf. 19th* 577-580.
- DONN, B., D. PEAK, S.-Y. LEE, E. FULLAR, AND L. DANKELMAN 1991. An experimental program to study impacts on compressible aggregates. *Lun. Planet. Sci. Conf. XXI*, 298-299. [Abstract]
- EVANS, D. L., AND S. V. KING 1966. Random network model of vitreous silica. *Nature* **212**, 1353-1354.
- GOLDREICH, P., AND W. R. WARD 1973. The formation of planetesimals. *Astrophys. J.* **183**, 1051-1061.
- HARTMANN, W. K. 1978. Planet formation: mechanism of early growth. *Icarus* **33**, 50-61.
- JOHNSON, K. L. 1985. *Contact Mechanics*. Cambridge Univ. Press, Cambridge.
- LELL, P., E. IGENBERGS, AND H. KUCZERA 1983. An electromagnetic accelerator. *J. Phys. E*, **16**, 325-330.
- MARKIEWICZ, W. J., AND J. BLUM 1993. Effects of collisional fragmentation and grain morphology on the growth of grains in the presolar nebula. Submitted for publication.
- MILLER, J. B., AND B. C. CLARK 1987. Feasibility study for gas-grain simulation facility. *NASA Conference Publication 10026*, pp. 3-48.
- MIZUNO, H., W. J. MARKIEWICZ, AND H. J. VÖLK 1988. Grain growth in turbulent proto-planetary accretion disks. *Astron. Astrophys.* **195**, 183-192.
- RYAN, E. V., W. K. HARTMANN, AND D. R. DAVIS 1991. Impact experiments. 3. Catastrophic fragmentation of aggregate targets and relation to asteroids. *Icarus* **94**, 283-298.
- SAFRONOV, V. S. 1969. Evolution of the protoplanetary cloud and formation of the earth and the planets. *NASA TTF-677*, 1972.
- VÖLK, H. J., F. C. JONES, G. E. MORFILL, AND S. RÖSER 1980. Collisions between grains in a turbulent gas. *Astron. Astrophys.* **85**, 316-325.
- WEIDENSCHILLING, S. J. 1984. Evolution of grains in a turbulent solar nebula. *Icarus* **60**, 553-567.
- WEIDENSCHILLING, S. J. 1988. Formation processes and time scales for meteorite parent bodies. In *Meteorites and the Early Solar System* (J. F. Kerridge and M. S. Matthews, Eds.), pp. 348-371, Univ. of Arizona Press, Tucson.
- WEIDENSCHILLING, S. J., AND J. N. CUZZI 1993. Formation of planetesimals in the solar nebula. In *Protostars and Planets III* (E. Levy, J. Lunine, and M. S. Matthews, Eds.), pp. 1031-1060, Univ. of Arizona Press, Tucson.